Bulletin of Engineering Geology and the Environment (2022) 81:434
https://doi.org/10.1007/s10064-022-02891-w

ORIGINAL PAPER

# Mechanical properties and fracture mode transformation of rocks subjected to asymmetric radial stresses

**Honggang Zhao[1,2,3] · Huang Gun[2,3] · Changbao Jiang[2,3] · Chao Liu[2,3,4]**

Received: 2 July 2021 / Accepted: 19 August 2022 / Published online: 20 September 2022


## Abstract

Based on the analysis of the radial stress distribution in surrounding rocks of tunnel, different asymmetric radial stresses were loaded, which can more truly reflect the stress state of surrounding rocks of tunnel. The stress state and boundary conditions of representative surrounding rock element were simulated by sandstone in this study. The mechanical response and fracture mode transformation were studied. The experimental results showed that as the depth of surrounding rocks from the free surface of tunnel increased, the properties of surrounding rocks showed the characteristics of transition from brittleness to ductility. The strengths of sandstone specimens gradually increased with the increase of the depth, and a power function can well characterize the relationship between the strength and the depth. The fracture modes of sandstone specimens transformed from tensile splitting fracture to tensile-shear complex fracture, and finally to shear fracture with the increase of the depth, which was mainly caused by the asymmetric radial stresses. According to the characteristics of fracture modes under different asymmetric radial stress conditions, four types of failure zones in the radial direction of surrounding rocks can be divided, i.e., tensile splitting failure zone, tensile-shear complex failure zone, shear failure zone, and slight shear failure zone. The shear fracture in deep surrounding rocks and the accompanying large deformation of surrounding rocks should be paid more attention in the support of tunnel. In addition, the accuracy of time-failure model was verified, and it can accurately predict the time needed for rock failure.

**Keywords** Asymmetric radial stress · Transformation · Fracture mode · Shear fracture · Time-failure model

## Introduction

With the gradual depletion of shallow resources and the development of underground constructions, the excavation of the tunnel gradually develops to the deep. More and more attentions have been paid to the stability of deep tunnel surrounding rocks. As we know that after tunnel excavation, a free surface is formed, and the radial stress in surrounding rocks at the boundary of tunnel is approximately zero. With the increase of the distance from the excavation-free surface, the radial stress gradually increases and finally tends to far-field stress. The characteristics of radial stress distribution lead to that surrounding rocks in different depths from the excavation free surface are subjected to different radial stresses. The stress state of surrounding rocks changes from biaxial stress at the boundary of tunnel (Su et al. 2017b) to poly-axial stress state with one face free and other five faces constrained near the excavation boundary and finally to the true triaxial stress state at a certain depth. Figure 1 shows the radial stress distribution curve of surrounding rocks along the radial direction of a circular tunnel. Based on the Kirsch equations and filed observations, the value of radial stress at the excavation free surface is zero, and it increases nonlinearly with the increase of the distance from the free surface. The distribution of radial stress shows notable gradient variations, and the radial stress gradient is more obvious under high in situ stress conditions, especially when the difference between the far-filed principal stresses is large.

✉ Huang Gun
hg023@cqu.edu.cn

✉ Changbao Jiang
jcb@cqu.edu.cn

[1] Department of Military Installations, Army Logistics University of PLA, Chongqing 401311, China

[2] State Key Laboratory of Coal Mine Disaster Dynamics and Control, Chongqing University, Chongqing 400030, China

[3] School of Resources and Safety Engineering, Chongqing University, Chongqing 400030, China

[4] School of Mechanics and Civil Engineering, China University of Mining and Technology, Xuzhou, China

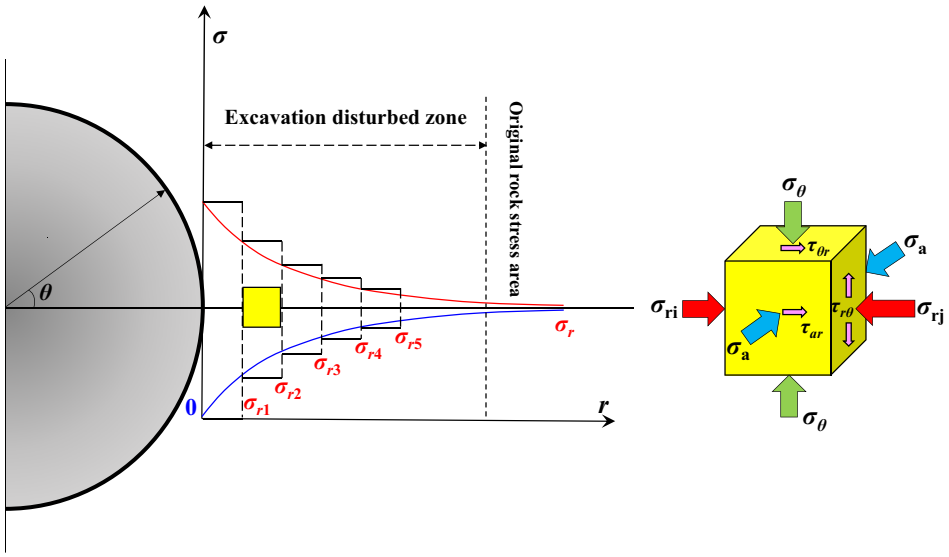


**Fig. 1** Radial stress distribution along the $\theta=0°$ direction ($\theta$ is the angular direction that rotates counterclockwise from the x-coordinate)

Extensive studies have been conducted on the mechanical behavior of surrounding rocks, and a large number of loading or unloading tests under uniaxial, biaxial, conventional triaxial, and true triaxial stress conditions have been carried out (Chen et al. 2009; Feng et al. 2016; Hua and You 2001; Huang and Li 2014; Jingtao and Xiating 2006; Yun et al. 2010a). In these studies, true triaxial tests considering the free surface have become the preferred method for investigating the stability of tunnel, especially the problems of rockburst (He et al. 2007, 2010, 2012a, b; Su et al. 2017a; Zhao and Cai 2014). The results of true triaxial tests considering the free surface show that this poly-axial stress state near the excavation boundary significantly affects the mechanical behavior, deformation, and energy characteristics of surrounding rocks (Alejano and Alonso 2005; Diederichs 2007; Zhao and Cai 2010a, b). He et al. (2010) unloaded the minimum principal stress and simulated the process of rockburst under different true triaxial stresses. The characteristics of rockburst and acoustic emission (AE) signals were studied. The experimental results showed that the stress level before unloading and unloading rates has a significant effect on the occurrence time of rockburst and the compressive strength of rocks. A high stress level or an unloading rate can trigger transient and intense strainburst. AE signals showed that the AE activity and energy release rapidly increased from unloading to the occurrence of rockburst. True triaxial stress states of surrounding rocks with different radial stress gradients after tunnel excavation were simulated by Su et al. (2017b). The influences of radial stress gradients on the strainburst were studied from the aspects of failure process, compressive strength, failure mode, and the kinetic energy of fragments. The experimental results were helpful to better understand the mechanism of strainburst. Su et al. (2018) conducted true triaxial rockburst tests using an improved rockburst test system and analyzed the evolution characteristics of AE and sound signals during the rockburst process. They found that on the eve of rockburst, the main frequency of AE and sound signals showed a downward trend. The research results provided powerful information for the prediction of rockburst. The true triaxial tests under different initial stresses and unloading rates were carried out to investigate the mechanisms of the deformation and failure of marble (Xu et al. 2019). The test results implied that the damage degree of marble gradually increased with the increase of unloading strain rate, and the failure mode of marble changed from mixed shear and tensile failure to tensile failure. In addition, more transgranular cracks were observed through microscopic images. Due to excavation, the unloading effect was simulated through the true triaxial experiments under different confining pressures and unloading rates (Si and Gong 2020), and it was found that under the same unloading rate, the greater the initial confining pressure, the greater the compressive strength and stress drop after failure, and the more intense the rockburst.

So far, the stability of surrounding rocks has been studied by many researchers. However, most of these studies focused on the failure of surrounding rocks, which are at the free surface of tunnel or near it. In the actual situation, the damage induced by the structural instability, rockburst, and other dynamic disasters after the tunnel excavation is not only confined to the vicinity of the free surface, but also spreads to deep surrounding rocks (Feng et al. 2013; Li et al. 2012; Ortlepp 2001). The free surface will be formed after tunnel excavation, and the stress in surrounding rocks will be redistributed. Then, the radial stress $\sigma_r$ gradually increases with the increase of the distance

between surrounding rocks and free surface. In addition, due to the constraint of adjacent rock elements, the shear stress exists on the surface of representative rock element. When the tangential stress $\sigma_\theta$ exceeds the capacity of surrounding rocks, the rocks at free surface or even a certain depth may be damaged or even cause the rockburst. The above stress conditions considering the variation of radial stress appears in the non-principal stress space (Su et al. 2017b), and it allows the existence of shear stress on the surface of the representative rock element. Thus, as the distance from the free surface increases, the radial stress increases nonlinearly, which leads to that surrounding rocks are subjected to asymmetric radial stresses with unequal stresses at the two faces in the radial stress direction, as shown in Fig. 1. In Fig. 1, the radial stress $\sigma_{ri}$ is less than $\sigma_{rj}$, which causes the existence of the stress gradient in the rock.

However, there are few reports on the effect of radial asymmetric constraints on the mechanical properties and fracture modes of surrounding rocks. Generally, the rock mechanics tests show that the stresses at the two parallel faces are equal, e.g., $\sigma_{ri} = \sigma_{rj}$. It cannot truly reflect the stress state of surrounding rocks, which results in that the damage degree of the deep surrounding rocks is unknown when the spalling, splitting failure, or even rockburst occurs. Moreover, the support depth of tunnel is closely related to the damage degree of deep surrounding rocks. Therefore, it is necessary to carry out the experimental research to truly simulate the stress state of surrounding rocks in the radial stress direction and boundary conditions, so as to obtain the influences of radial asymmetric constrains on the mechanical properties, and fracture modes of surrounding rocks, and deepen the understanding of rockburst and the damage of deep surrounding rocks.

## Experimental preparation

### Specimen preparations

Sandstone specimens were used in this study to simulate surrounding rocks. The sandstone specimens are gray-white without obvious cracks, defects, or beddings on the surface. The homogeneity of them is good, and it can effectively reduce the test dispersion. Before taking the tests, the sandstone specimens are ground to cubes with 100 mm × 100 mm × 100 mm in length, width, and height, respectively. The squareness of each cube specimen surfaces is within 0.02 mm. The cube sandstone specimens are presented in Fig. 2. Before the test, the uniaxial compression and Brazilian splitting tests were carried out to obtain the basic physical parameters of sandstone, as shown in Table 1.

**Fig. 2** Cube sandstone specimens

### True triaxial equipment

A newly developed true triaxial equipment (TTG) by the Chongqing University in China was used in this study (Li et al. 2016). The 3D schematic diagram and physical diagram of TTG are shown in Fig. 3. In addition, the relationship between the loading heads in true triaxial cell and the rectangular coordinate system is shown in Fig. 3. Each stress loading head in true triaxial cell can independently load the specimen under the displacement or force control mode, which provides operability for the application of asymmetric true triaxial stress state in this study. Among the six stress loading heads, four stress loading heads in the X and Y directions can apply a maximum pressure of 6000 kN, and two stress loading heads in the Z directions can apply a maximum pressure of 4000 kN (Zhao et al. 2020). This system can truly simulate the stress path under different engineering backgrounds and fully meet the technical requirements of the tests in this study.

### Experimental scheme

The deep tunnel with a radius of $a$ and a buried depth of 1000 m is taken as an example. According to the existing research results (Gong et al. 2017, 2018; Luo et al. 2019, 2020), the vertical and horizontal principal stresses can be obtained through the calculation formula of in situ stress by Stephansson et al. (1986), and the expressions are as follows:

$$\begin{aligned} \sigma_v &= \gamma H \\ \sigma_h^{\max} &= 6.7 + 0.0444H \\ \sigma_h^{mix} &= 0.8 + 0.0329H \end{aligned} \quad (1)$$

**Table 1** Basic physical parameters of sandstone

| Specimen | UCS/MPa | Tensile strength/MPa | E/GPa | $v$ |
|---|---|---|---|---|
| Sandstone | 75.16 | 6.86 | 12.22 | 0.22 |

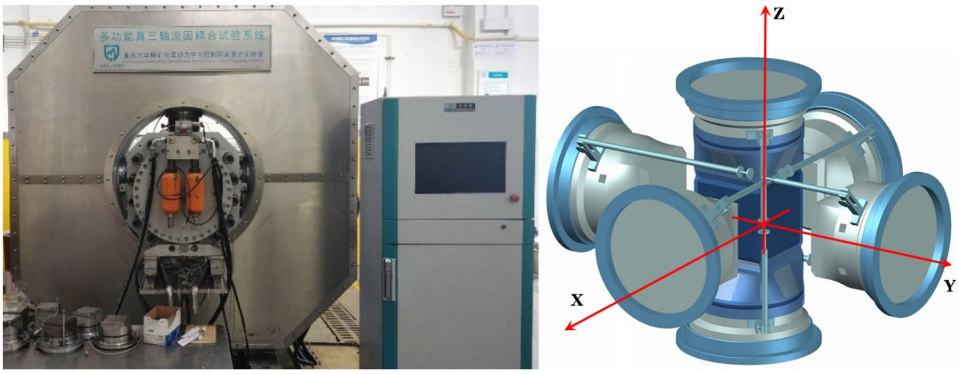


**Fig. 3** True triaxial equipment (TTG)

where $\gamma$ is the average bulk density of rock, and taking as 27kN/m$^3$, $H$ is the depth of tunnel, $\sigma_v$ is the vertical principal stress (MPa), $\sigma^{max}_h$ is the maximum horizontal principal stress (MPa), and $\sigma^{mix}_h$ is the minimum horizontal principal stress (MPa). According to Eq. (1), we can obtain that $\sigma_v = 27$ MPa, $\sigma^{max}_h = 51.1$ MPa, and $\sigma^{mix}_h = 33.7$ Mpa.

Generally, three ways of tunnel layout are applied in practical engineering, i.e., the axis of tunnel along the direction of $\sigma^{max}_h$, $\sigma^{mix}_h$, or along a angle with the direction of $\sigma^{max}_h$. In this study, the axis of tunnel along the $\sigma^{max}_h$ direction is taken as an example (Gong et al. 2018). Based on the Kirsch equations, the distribution of radial stress $\sigma_r$ around the tunnel excavation boundary can be calculated, and the curve of the distribution of radial stress $\sigma_r$ is shown in Fig. 4. According to the values of radial stresses $\sigma_r$, eight different ranges of surrounding rocks are divided along the direction of radial stress $\sigma_r$ with the increment of 5 MPa. In Fig. 4, the radial stress $\sigma_r$ expresses an obvious nonlinear increase. The value of radial stress $\sigma_r$ on the free surface of tunnel is zero. When the distance $L = 0.115a$, radial stress $\sigma_r$ is about 5 MPa; the distance $L = 0.257a$, radial stress $\sigma_r$ is about 10 MPa; the distance $L = 0.447a$, radial stress $\sigma_r$ is about 15 MPa; the distance $L = 0.733a$, radial stress $\sigma_r$ is about 20 MPa; the distance $L = 1.243a$, radial stress $\sigma_r$ is about 25 MPa; and the distance $L = 2.717a$, radial stress $\sigma_r$ is about 30 MPa. When the distance $L$ is greater than $2.717a$, the radial stress $\sigma_r$ gradually approaches to the far field stress 33 MPa. Due to the range of surrounding rocks where the radial stress $\sigma_r$ from 30 to 33 MPa is large, the radial stress $\sigma_r$ is set as 30 MPa in this range. It should be noted that the plane strain problem is considered by the Kirsch equations and the axis stress $\sigma_a$ along the axis of tunnel basically remains unchanged in the actual excavation process. Thus, the variation of axial stress $\sigma_a$ before and after excavation is not considered in this study.

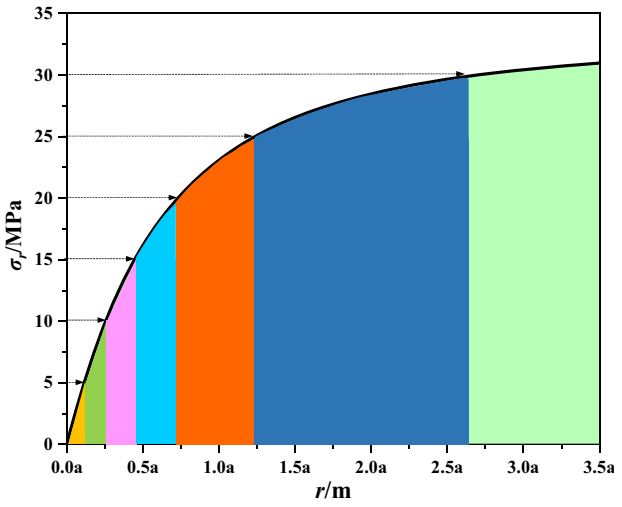


**Fig. 4** Radial stress distribution along the $\theta = 0°$ direction of the circular tunnel with buried depth of 1000 m

According to the above analyses, it can be seen that two faces of the rock element in the direction of radial stress are subjected to different radial stresses, and this special boundary condition is called asymmetric stress condition in our study in the non-principal stress space. Generally, the unloading in the process of tunnel excavation can easily cause the instability of surrounding rocks or even the rockburst. However, the formation of free surface and the increase of tangential stress in surrounding rocks are also the main factors that lead to the failure of surrounding rocks and rockburst. A large number of engineering practices show that the failure of surrounding rocks and rockburst induced by the increase of tangential stress often occur within a few hours or 1–3 days after tunnel excavation (Feng et al. 2013). Thus, the stress load path in this study is designed as follows:

Step 1: Load $\sigma_\theta$ and $\sigma_a$ to preset value with force control of 1 kN/s, while $\sigma_r$ is loaded to $\sigma_{ri}$ with force control of o.5 kN/s.
Step 2: Continually load $\sigma_\theta$ and $\sigma_a$. Keep $\sigma_{ri}$ on one face of specimen unchanged and increase the stress on the opposite face to $\sigma_{ji}$.

Step 3: Keep $\sigma_a$, $\sigma_{ri}$, and $\sigma_{ji}$ constant and continually increase $\sigma_\theta$ with displacement control of 0.001 mm/s until specimen failure.

For convenience, in the following analysis, $\sigma_z$, $\sigma_y$, and $\sigma_x$ are used to represent $\sigma_\theta$, $\sigma_a$, and $\sigma_r$, respectively. The schematic diagram of experimental scheme and stress loading curve under the stress condition of $\sigma_{xi}=5$ MPa and $\sigma_{xj}=10$ MPa are shown in Fig. 5. The specific experimental scheme is shown in Table 2.

**Table 2** Experiment plan

| Specimen no | $\sigma_y$/MPa | $\sigma_{xi}$/MPa | $\sigma_{xj}$/MPa |
|---|---|---|---|
| RSG1 | 50 | 0 | 0 |
| RSG2 | 50 | 0 | 5 |
| RSG3 | 50 | 5 | 10 |
| RSG4 | 50 | 10 | 15 |
| RSG5 | 50 | 15 | 20 |
| RSG6 | 50 | 20 | 25 |
| RSG7 | 50 | 25 | 30 |
| RSG8 | 50 | 30 | 30 |

## Experimental results and analysis

### Stress–strain curves of sandstone specimen under different asymmetric radial stress conditions

Figure 6 shows the stress–strain curves under different asymmetric radial stress conditions. As shown in Fig. 6, since the cracks in the sandstone specimens have been compacted during the stage of initial stress loading, the stage of crack compaction in the stress–strain curve under different asymmetric radial stress conditions is not obvious. Table 3 lists the drop amplitudes and the rates of stress decrease under different asymmetric radial stress conditions. It can be seen that when $\sigma_{xi}$ was loaded to 0 ~ 15 MPa and $\sigma_{xj}$ was loaded to 0 ~ 20 MPa, the stress decline was obvious after the stress reached the peak and the drop amplitude was great. It indicated that a intense brittle failure of sandstone specimen occurred. When $\sigma_{xi}$ was loaded to 20 ~ 30 MPa and $\sigma_{xj}$ was loaded to 25 ~ 30 MPa, the rate of stress drop was low, and the drop amplitude was small. This phenomenon was the most obvious when $\sigma_{xi}=25$ MPa, $\sigma_{xj}=30$ MPa and $\sigma_{xi}=30$ MPa, $\sigma_{xj}=30$ MPa. The sandstone specimen expressed obvious ductility characteristics. To quantitatively described the brittleness or ductility of sandstone specimen, the brittleness index was proposed by Bishop (1967) and denoted by $K$. The expression is as follows:

$$K=\frac{\sigma_{zp}-\sigma_{zr}}{\sigma_{zp}}\times 100\% \tag{2}$$

where $\sigma_{zp}$ is the peak stress (MPa) and $\sigma_{zr}$ is the residual strength (MPa).

According to Eq. (2), we obtained the brittleness indexes $K$ of surrounding rocks at different depths from the free surface, and the columnar diagram of brittleness indexes $K$ was shown in Fig. 7. $a$ represents the radius of tunnel. From Fig. 7, it can be found that the brittleness of surrounding rocks near the free surface was relatively large, which led to a intense failure of surrounding rocks. With the increase of $L$, the brittleness indexes $K$ gradually decreased, the ductility of surrounding rocks performed more obviously. To sum up, with the increase of $L$, the properties of surrounding rocks showed a characteristics of transformation from brittleness to ductility.

From Fig. 6b, the strain of sandstone specimen near the free surface (i.e., $\sigma_{xi}=\sigma_{xj}=0$ MPa and $\sigma_{xi}=0$, $\sigma_{xj}=5$ MPa) was positive in the $\sigma_y$ direction which implied that the compression deformation dominated the deformation of surrounding rocks in the $\sigma_y$ direction. When $\sigma_{xi}\geq 5$ MPa and $\sigma_{xj}\geq 10$ MPa, the strain of sandstone specimen in the $\sigma_y$ direction was negative. It indicated that the deformation of surrounding rocks which was far away from the free

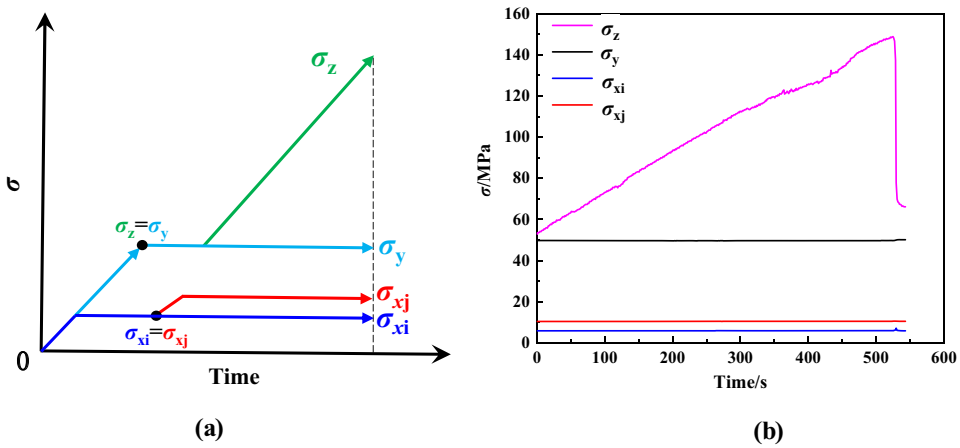


**Fig. 5** Stress loading curves: **a** schematic diagram of experimental scheme; **b** stress loading curve under the stress condition of $\sigma_{xi}=5$ MPa and $\sigma_{xj}=10$ MPa

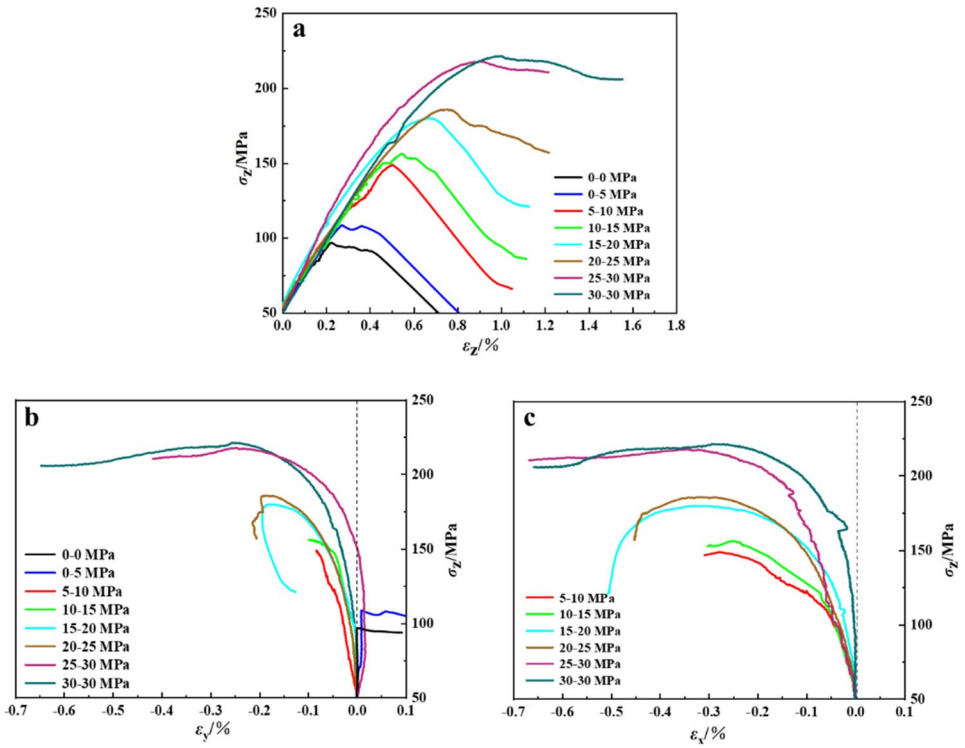


**Fig. 6** Stress–strain curves under different asymmetric radial stress conditions: **a** stress–strain curve in the tangential direction ($\sigma_z$); **b** stress–strain curve in the axial direction ($\sigma_y$); and **c** stress–strain curve in radial direction ($\sigma_x$)

surface mainly exhibited tensile expansion in the $\sigma_y$ direction. Compared with Fig. 6b and c, we can find that the surrounding rock which was far away from the free surface exhibited tensile expansion in the horizontal direction, and under the same stress condition, the tensile expansion of sandstone specimen in the $\sigma_x$ direction was greater than that in the $\sigma_y$ direction. Figure 8 shows the absolute values of the strain difference $\Delta\varepsilon$ between $\varepsilon_x$ and $\varepsilon_y$ under different stress conditions. It can be observed that $\Delta\varepsilon$ gradually decreased with the increase of $\sigma_{xi}$ and $\sigma_{xj}$, which indicated that the tensile expansion in the $\sigma_y$ direction was gradually close to that in the $\sigma_x$ direction. That was to say, with the increase of the distance $L$ from the free surface, the expansion deformation of surrounding rocks in the horizontal direction changed from mainly concentrated in the $\sigma_x$ direction to the uniform distribution in the $\sigma_x$ and $\sigma_y$ direction.

## Characteristics stresses of sandstone under different asymmetric radial stress conditions

The characteristic stresses of surrounding rocks, including the peak strength of surrounding rocks $\sigma_{zp}$, the crack initiation stress $\sigma_{ci}$, and the damage stress $\sigma_{cd}$, are helpful to understand the damage degree of surrounding rocks along the radial direction. In this study, the strengths of sandstone specimens were the overall response of rock under different asymmetric radial stress conditions, which can truly reflect the bearing capacity of surrounding rocks within a certain depth from the free

**Table 3** Drop amplitudes and rates of stress decrease under different radial stress conditions

| Specimen number | $\sigma_{xi}$/MPa | $\sigma_{xj}$/MPa | $L$ | $\sigma_{zp}$/MPa | $\sigma_{zr}$/MPa | $\sigma_{da}$/MPa | $v_{da}$/MPa·s$^{-1}$ |
|---|---|---|---|---|---|---|---|
| S1 | 0 | 0 | 0 | 96.75 | 27.59 | 69.16 | 2.03 |
| S2 | 0 | 5 | 0.058$a$ | 108.45 | 31.85 | 76.60 | 1.96 |
| S3 | 5 | 10 | 0.186$a$ | 148.73 | 66.01 | 82.72 | 2.16 |
| S4 | 10 | 15 | 0.352$a$ | 156.07 | 85.76 | 70.31 | 0.96 |
| S5 | 15 | 20 | 0.590$a$ | 179.90 | 120.62 | 59.28 | 1.03 |
| S6 | 20 | 25 | 0.988$a$ | 185.88 | 157.15 | 28.73 | 0.19 |
| S7 | 25 | 30 | 1.980$a$ | 217.83 | 209.14 | 8.69 | 0.06 |
| S8 | 30 | 30 | 2.717$a$ | 221.35 | 205.22 | 16.13 | 0.07 |

Drop amplitudes and rates of stress decrease are expressed by $\sigma_{da}$ and $v_{da}$, respectively

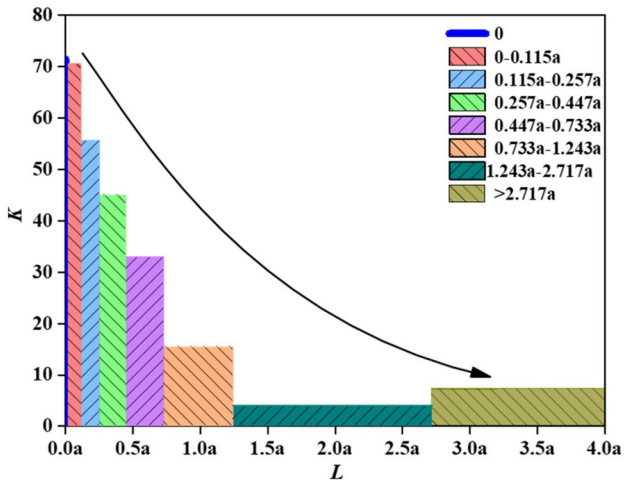


**Fig. 7** Columnar diagram of brittleness indexes $K$

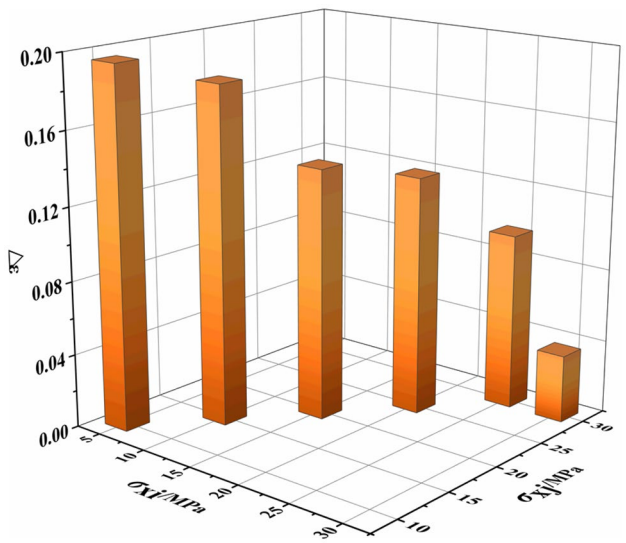


**Fig. 8** Absolute values of the strain difference $\Delta\varepsilon$ between $\varepsilon_x$ and $\varepsilon_y$ under different stress conditions

surface. Table 3 lists the sandstone strengths under different asymmetric radial stress conditions. In Table 3, when $\sigma_{xi} = \sigma_{xj} = 0$ MPa, i.e., the surrounding rock at the free surface of tunnel, the strength of sandstone specimen was the lowest (96.75 MPa). With the increase of $\sigma_{xi}$ and $\sigma_{xj}$, the strength gradually increased. When $\sigma_{xi}$ and $\sigma_{xj}$ increased to 30 MPa, i.e., the surrounding rock was in the original rock stress area, the strength was the largest (221.35 MPa). This was consistent with the previous results that the rock strength increased with the increase of confining pressure or minimum horizontal principal stress (Horii and Nemat-Nasser 1985). However, the stress constraint conditions in our study were obviously different from those applied in the previous conventional triaxial or true triaxial mechanical tests, which more truly reflected the strength characteristics of surrounding rock within a certain depth from the free surface.

In addition, in Table 3, we can see that the strength of S8 was greater than that of S7. The sandstone specimen (S7) was considered to consist of four thin rock plates (1–4 in Fig. 9). Due to the fact that there was a stress gradient in the specimen, the stress acting on the rock plate in the $\sigma_x$ direction gradually increased, resulting in a gradient change of its strength. The strength of rightmost rock plate (4) was approximately equal to that of S8, and the strengths of other three rock plates were less that that of S8. Thus, when the four thin rock plates were combined into a whole rock (S7), the strength was less than that of S8.

The in situ brittle failure of tunnel surrounding rocks usually occurs near the excavation boundary and gradually develops along the radial direction to deep surrounding rocks. Previous studies have shown that the surrounding rock failure or rockburst caused by the tangential stress concentration not only occurred near the excavation free surface, but also caused different degrees of damage in deep surrounding rocks. Generally, the failure process of rock materials is usually accompanied by crack closure and propagation. Base on the characteristics of crack deformation, the mode of crack strain was proposed by Martin (1997), and it is widely used to identify the crack initiation stress $\sigma_{ci}$ and crack damage stress $\sigma_{cd}$ at present (Cai et al. 2004; Wang et al. 2012). According to the mode of crack strain, the crack strain is equal to the measured strain minus the elastic strain, as shown in Eq. (3).

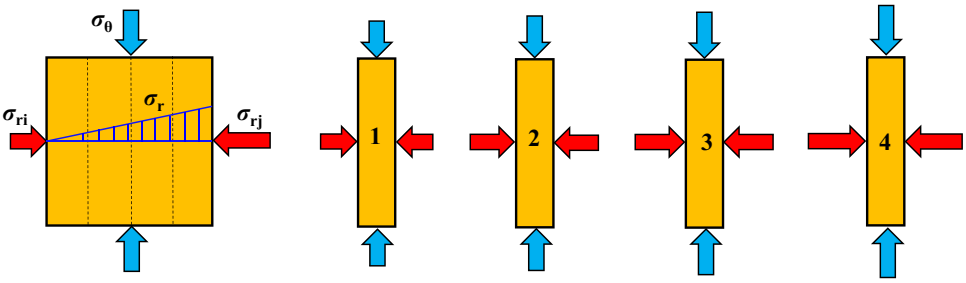


**Fig. 9** Schematic diagram of rock strength change under asymmetric radial stress conditions

$$\begin{aligned}
\varepsilon_z^c &= \varepsilon_z - \frac{1}{E}\left[\sigma_z - v\left(\sigma_y + \sigma_x\right)\right] \\
\varepsilon_y^c &= \varepsilon_y - \frac{1}{E}\left[\sigma_y - v\left(\sigma_z + \sigma_x\right)\right] \\
\varepsilon_x^c &= \varepsilon_x - \frac{1}{E}\left[\sigma_x - v\left(\sigma_z + \sigma_y\right)\right] \\
\varepsilon_v^c &= \varepsilon_z^c + \varepsilon_y^c + \varepsilon_x^c = \varepsilon_v - \frac{1-2v}{E}\left(\sigma_z + \sigma_y + \sigma_x\right)
\end{aligned} \tag{3}$$

where $\varepsilon_z$, $\varepsilon_y$, and $\varepsilon_x$ are the measured strains in the directions of $\sigma_z$, $\sigma_y$, and $\sigma_x$, respectively. $\varepsilon^c{}_z$, $\varepsilon^c{}_y$, and $\varepsilon^c{}_x$ are the crack strains in the directions of $\sigma_z$, $\sigma_y$, and $\sigma_x$, respectively. $\varepsilon_v$ is the measured volumetric strain, and $\varepsilon^c{}_v$ is the volumetric crack strain.

Figure 10 shows the measured volumetric strain and crack volumetric strain of sandstone during the compression failure under asymmetric radial stress conditions. According to Fig. 10, the process of rock failure can be divided into four stages: stage I—the cracks gradually close. Stage II—in this stage, only elastic compression deformation occurs, which is shown as a horizontal straight line on the crack volumetric strain, i.e., line AB in Fig. 10. When the existing cracks in rock propagate and the new cracks appear, the measured volumetric strain includes elastic volumetric strain and crack volumetric strain, which makes the curve of crack volumetric strain begin to deviate from the straight line, i.e., point B in Fig. 10. The stress corresponding to the deviation point is the crack initiation stress $\sigma_{ci}$. The stage III is the steady growth stage of cracks. In this stage, the cracks in the rock gradually increase, and the crack volumetric strain shows the effect of propagation and increase. At the end of this stage (point C), the prototype of shear plane begins to form in the rock, and the cracks begin to unsteadily propagate. The expansion deformation in the horizontal direction is greater than the compression deformation in the vertical direction, which leads to the appearance of the inflection point (point D) of the measured volumetric strain curve. The stress corresponding to this inflection point is the crack damage stress $\sigma_{cd}$.

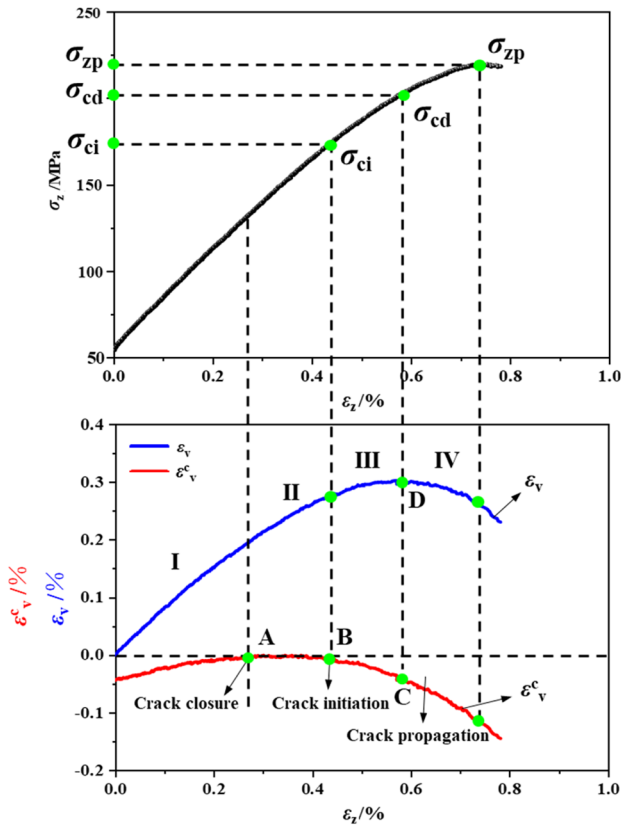


**Fig. 10** Curves of the measured volumetric strain $\varepsilon_v$ and crack volumetric strain $\varepsilon^c{}_v$

According to the above method, $\sigma_{xi}$ and $\sigma_{xj}$ can be obtained, as shown in Table 4. Due to the fact that the strain in the $\sigma_x$ direction cannot be measured, $\sigma_{ci}$ and $\sigma_{cd}$ under the stress condition of $\sigma_{xi} = 0$ MPa and $\sigma_{xj} = 5$ MPa were not shown in Table 4.

The mean values of the ranges of surrounding rocks corresponding to different $\sigma_{xi}$ and $\sigma_{xj}$ were caculated. For example, the surrounding rock under the stress condition of $\sigma_{xi} = 5$ MPa and $\sigma_{xj} = 10$ MPa was located in the range of $0.115a \sim 0.257a$ from the free surface, then the mean value of this range was taken, i.e., the distance $L$ of the surrounding rock from the free surface is $0.186a$, as shown in Table 4. Thus, the relationship between the distance $L$ and the strength of surrounding rock, the measured volumetric strain, and crack volumetric strain of sandstone were obtained, as shown in Fig. 11. It can be seen that the characteristic stresses gradually increased with the increase of $L$, which indicates that the restraining effect of the depth of surrounding rocks on crack initiation and propagation is gradually strenthened. When $L$ increased from 0.186a to 0.988a, the values of $\sigma_{zp}$, $\sigma_{ci}$, and $\sigma_{cd}$ increased by 37.15 MPa, 32.04 MPa, and 44.66 MPa, respectively. When $L$ increased from 0.988a to 2.717a, the values of $\sigma_{ci}$ and $\sigma_{cd}$ increased by 35.47 MPa, 28.38 MPa, and 40.04 MPa, respectively. This phenomenon indicates that

**Table 4** Crack initiation stress $\sigma_{ci}$ and damage stress $\sigma_{cd}$ under different radial stress conditions

| Specimen number | $\sigma_{xi}$/MPa | $\sigma_{xj}$/MPa | $L$ | $\sigma_{ci}$/MPa | $\sigma_{cd}$/MPa |
|---|---|---|---|---|---|
| S3 | 5 | 10 | 0.186$a$ | 108.66 | 115.51 |
| S4 | 10 | 15 | 0.352$a$ | 116.86 | 127.74 |
| S5 | 15 | 20 | 0.590$a$ | 134.95 | 154.59 |
| S6 | 20 | 25 | 0.988$a$ | 140.70 | 160.17 |
| S7 | 25 | 30 | 1.980$a$ | 166.26 | 196.03 |
| S8 | 30 | 30 | 2.717$a$ | 169.08 | 200.21 |

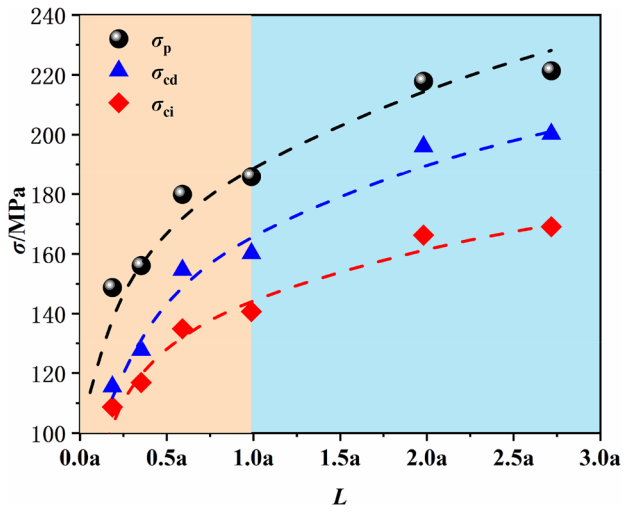


**Fig. 11** Variation curves of characteristic stresses of surrounding rocks at different depth from excavation free surface

the rate of increase of the characteristic stresses in shallow surrounding rocks is higher that in deep surrounding rocks. This result can be explained by the rough contact model of primary cracks in surrounding rocks, as shown in Fig. 12a.

It can be assumed that the primary crack surfaces are saw-tooth shaped. When the distance between the surrounding rock and free surface is small, the primary cracks are affected by low confinement (low $\sigma_r$). Rock elements will slide along the slope of serrated boss, resulting in dilatancy, which leads to crack initiation and propagation. In this case, there is no cohesive force on the surface of crack, and the resistance $\tau_R$ against the relative slide between crack surfaces can be expressed as

$$\tau_R = \sigma_n \tan(\phi_b + \alpha) \tag{4}$$

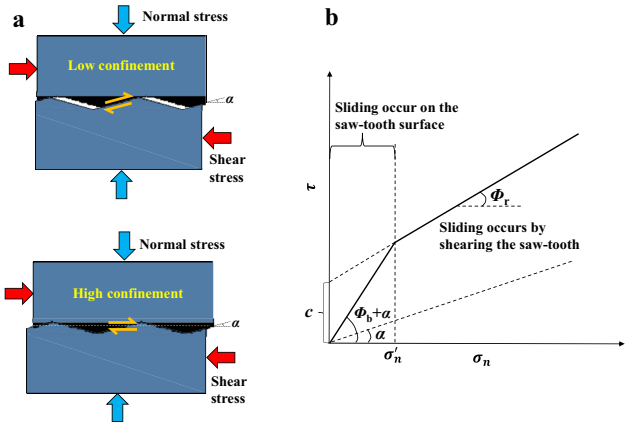


**Fig. 12** Schematic diagram of crack initiation and propagation model of fractured rock under different constraint effects

where $\sigma_n$ is the normal stress, $\Phi_b$ is the basic friction angle of the crack surface, and $a$ denotes the ramp angle of boss. When the constraint effect reaches the critical value, the serrated boss will be sheared, that is to say, the intact rock will be sheared, and the dilatancy will disappear. In this case, $\tau_R$ can be expressed as

$$\tau_R = c + \sigma_n \tan \phi_r = \sigma_n' \tan(\phi_b + \alpha) + (\sigma_n - \sigma_n') \tan \phi_r \tag{5}$$

where $c$ is the cohesive force of intact rock, $\Phi_r$ is the residual friction angle of intact rock, and $\sigma_n'$ is the normal stress that corresponds to the critical confinement. According to Eqs. (4) and (5), when $\sigma_n$ is limited at a low level, the increase of $\tau_R$ is mainly dependent on $\Phi_b + a$, while when $\sigma_n$ is at a high level, the increase of $\tau_R$ is dependent on $\Phi_r$. In this section, the axial stress is fixed, and the radial stress $\sigma_{xi}$ and $\sigma_{xj}$ dominate the change of constraint effect, and the constraint effect on the primary crack increases with the increase of $\sigma_{xi}$ and $\sigma_{xj}$. Since $\Phi_b + a$ is significantly greater than $\Phi_r$ (Fig. 12b), when $\sigma_{xi}$ and $\sigma_{xj}$ increase at a low stress level, the resistance to crack initiation and propagation will increase at a high rate. Thus, when $\sigma_{xi}$ and $\sigma_{xj}$ increase at a low stress level, the rates of the increase of the characteristic stresses are greater than those at a high stress level.

According to the results of the above analyses, the characteristic stresses of surrounding rocks along the radial direction can be summarized as follows: with the increase of the depth from the free surface, the characteristic stresses of surrounding rocks gradually increase, and the surrounding rock at or near the free surface is more susceptible to the radial stress than that far away from the free surface. According to the magnitude of the radial stress, the tunnel can be roughly divided into two regions along the radial direction: region 1 ($\sigma_{xi}$ and $\sigma_{xj}$ are relatively small) and region 2 ($\sigma_{xi}$ and $\sigma_{xj}$ is relatively large). Compared with region 2, the increase rates of characteristic stresses in region 1 are higher with the increase of radial stress. It should be noted that the division of region 1 and region 2 needs to determine the characteristic stresses of surrounding rocks according to the specific stress environment and lithology. For example, in this chapter, according to Fig. 11, the critical depth of region 1 is about 0.590a ~ 0.988a.

## Fracture mode of sandstone under different asymmetric radial stress conditions

Figure 13 shows the physical images and CT scanning diagrams of fracture modes under different asymmetric radial stress conditions after sandstone specimen failure. It needs to be noted that since the sandstone specimen under the stress condition of $\sigma_{xi}$ and $\sigma_{xj} = 0$ MPa is seriously damaged, the fracture mode can be clearly observed by using binary image instead of CT scanning diagram. As it can be seen from

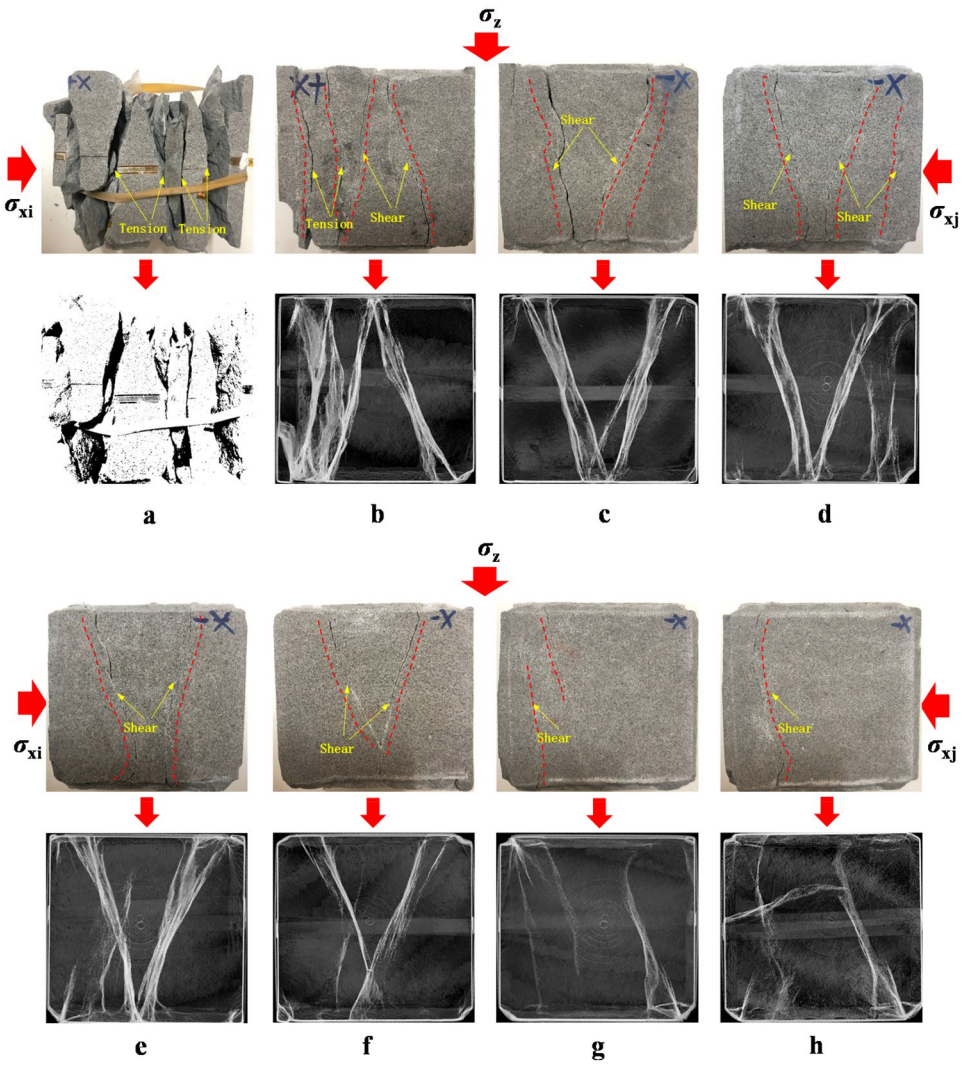


**Fig. 13** Failed specimens under different asymmetric radial stress conditions: (**a**) $\sigma_{xi}=0$ MPa, $\sigma_{xj}=0$ MPa; (**b**) $\sigma_{xi}=0$ MPa, $\sigma_{xj}=5$ MPa; (**c**) $\sigma_{xi}=5$ MPa, $\sigma_{xj}=10$ MPa; (d) $\sigma_{xi}=10$ MPa, $\sigma_{xj}=15$ MPa; (**e**) $\sigma_{xi}=15$ MPa, $\sigma_{xj}=20$ MPa; (**f**) $\sigma_{xi}=20$ MPa, $\sigma_{xj}=25$ MPa; (**g**) $\sigma_{xi}=25$ MPa, $\sigma_{xj}=30$ MPa; (**h**) $\sigma_{xi}=30$ MPa, $\sigma_{xj}=30$Mpa

Fig. 13, the fracture modes of sandstone specimens showed obvious differences under different $\sigma_{xi}$ and $\sigma_{xj}$. In this test, the distributions of $\sigma_x$ simulated the stress conditions of surrounding rocks in the radial direction, which were located in an area from the free surface to the original rock stress area. The two opposite faces of sandstone specimen were subjected to different radial stresses $\sigma_x$, i.e., $\sigma_{xi} \le \sigma_{xj}$, which led to the different fracture modes of surrounding rocks located near and far away from the free surface. In our study, the tensile fractures are characterized by smooth surface of fracture and few powders or small grains distribution, and the coarse fractures with a large amount of powders or small grains are regarded as shear fractures (Haimson 2007).

The results in Fig. 13 showed that under biaxial compression, the fracture modes of sandstone specimens exhibited tensile splitting failure. Several splitting fractures appeared in sandstone specimen along the $\sigma_x$ direction, and rock plates which approximately parallel to the $\sigma_z$ and $\sigma_y$ direction or the free surface were formed. This was consistent with the previous experimental results that focused on the failure of surrounding rocks near the excavation boundary (Cai 2008; Diederichs 2007; Gong et al. 2012; Read and Martin 1996; Yun et al. 2010b).

The fracture mode of sandstone specimen under the stress condition of $\sigma_{xi}=0$ MPa and $\sigma_{xj}=5$ MPa is presented in Fig. 13b. In this case, near the free surface, several splitting fractures through the specimen appeared, while the shear fractures were formed far away from the free surface. Since the stress gradient existed in the sandstone specimen in the $\sigma_x$ direction, we considered the specimen as a geometry consisting of four thinner rock plates, as shown in Fig. 14a. The first rock plate, which was near the free surface, was subjected to small radial stress and was almost in a state of approximate biaxial compression stress. Therefore, the strength of the first rock plate was low and easy to form the tensile cracks. When the tensile cracks spread through the

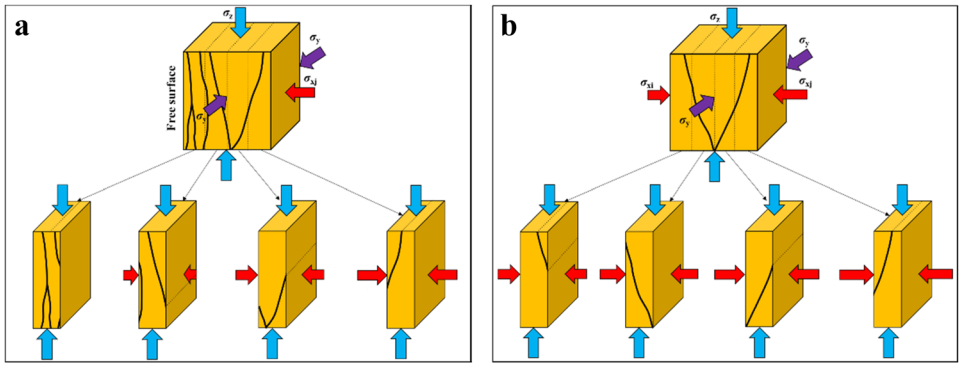


**Fig. 14** Schematic diagram of fracture mode transformation

sandstone specimen, the split rock plates were formed as shown in Fig. 14a. As the distance of the rock plates from free surface increased, rock plates were subjected to a large stress. The stress state can be regarded as true triaxial stress state. Thus, the rock strength was relatively large, and the formation of tensile cracks was inhibited, and shear fractures were more likely to generate (Feng et al. 2016; Haimson and Chang 2000; Hoek and Martin 2014), as shown in Figs. 13b and 14b. Therefore, the fracture mode of sandstone specimen under the stress condition of $\sigma_{xi}=0$ MPa and $\sigma_{xj}=5$ MPa exhibited tensile-shear complex failure.

When $\sigma_{xi}$ was in the range of 5 ~ 20 MPa and $\sigma_{xj}$ was in the range of 10 ~ 25 MPa, it can be seen in Fig. 13c ~ f that the ultimate failure of sandstone specimens was mainly dominated by the shear fractures. The main reason for this phenomenon might be that when $\sigma_{xi}$ and $\sigma_{xj}$ are relatively large, the four rock plates are all in a true triaxial stress condition (Fig. 14b). The initiation and propagation of tensile cracks in the $\sigma_x$ direction are effectively restrained, so that all rock plates exhibit shear fracture (Feng et al. 2020), which results in shear failure of sandstone specimen as a whole.

When $\sigma_{xi}$ and $\sigma_{xj}$ increased close to the far-filed stress, i.e., $\sigma_{xi}=25$ MPa, $\sigma_{xj}=30$ MPa and $\sigma_{xi}=30$ MPa, $\sigma_{xj}=30$ MPa, the number of fractures on the surface of sandstone specimens was relatively less, and the length of them was short. Through CT scanning and three-dimensional reconstruction of sandstone specimens under the above stress conditions (Fig. 15), we found that in the $\sigma_x$ direction, the shear fractures appeared on both front and back surfaces of sandstone specimen. But these fractures did not fully coalesce to form the macroscopic fracture surface, and the degree of sandstone failure was relatively low. This might be due to that the micro tensile cracks in the rock have almost the same opportunity to expand along the $\sigma_{xi}$ and $\sigma_{xj}$ directions. However, due to the great constraint, the crack propagation time is short. After the cracks coalesce, the slight shear fractures are formed along the $\sigma_{xi}$ and $\sigma_{xj}$ directions.

According to the above analyses, it can be seen that with the increase of the distance $L$, the fracture modes of sandstone specimens varied significantly and gradually changed from tensile splitting failure at the boundary of free surface to tensile-shear complex failure near the free surface, and then to shear failure at a certain depth from the free surface, and finally to slight shear failure in the area which was close to the original rack stress area. This kind of variation of fracture modes had a good consistency with the failure mode of surrounding rock after tunnel instability or rockburst in the field (Jiang 2017). Based on the transformation of fracture modes under different asymmetric radial stress conditions, the four types of failure zones of surrounding rocks in the

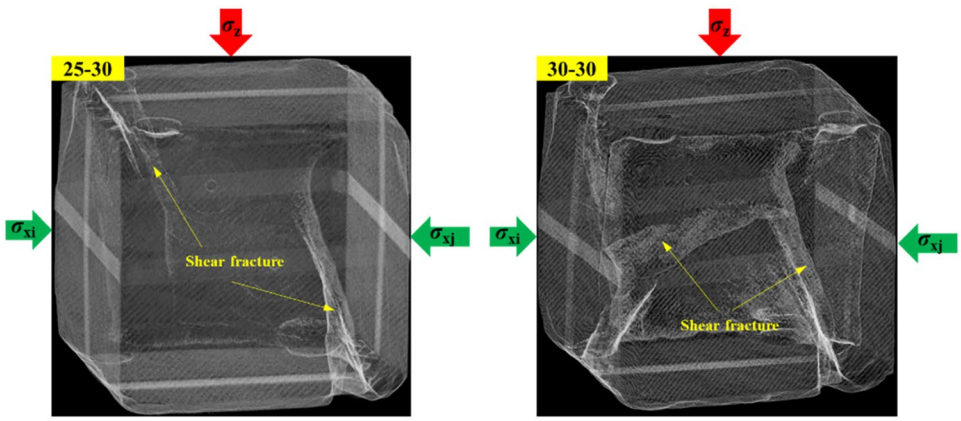


**Fig. 15** Three-dimensional reconstruction of failed specimens

radial direction were divided, i.e., tensile splitting failure zone, tensile-shear complex failure zone, shear failure zone, and slight shear failure zone, as shown in Fig. 16.

It should be noted that we need to pay more attention to the shear fracture in our tests. When the tangential stress is large enough, the surrounding rocks at and near the free surface will be destroyed first, forming the split rock plates. As the tangential stress continues to increase, the size of rock plates reaches its bucking size, and then it is broken, and the rock fragments are ejected into the tunnel space, resulting in a strong dynamic failure phenomenon, i.e., rockburst. Finally, the rockburst pits are formed on the surface of tunnel, as shown in Fig. 17a. At this time, the shear fractures induced by the relatively large tangential stress may be formed in deep surrounding rock, and the residual elastic energy in the surrounding rock is great. Thus, damage range of surrounding rocks caused by rockburst is not only limited to the depth of rockburst pits, but also extends to deep surrounding rocks, as shown in Fig. 17b. The tunnel with a radius of $a$ is taken as an example, and we assume that the formation of rockburst pits is caused by the fracture of rock plates. According to Fig. 13b, the range of tensile splitting is about one-third of the total width of sandstone specimen. Thus, it can be calculated that the range of tensile splitting near the free surface is about $0 \sim 0.0383a$, i.e., the depth of rockburst spits is $0.0383a$. The depth of surrounding rocks with shear fracture is greater than $0.0383a$. Therefore, in the support of tunnel surrounding rocks, it is not only necessary to strengthen surrounding rocks near the free surface to avoid the tensile splitting fracture caused by high tangential stress in the tunnel support, but also to pay more attention to the shear fracture in deep surrounding rocks and the accompanying large deformation of surrounding rocks.

## Discussion

### Analysis of progressive damage process of surrounding rock under asymmetric radial stress conditions

During tunnel excavation, the surrounding rocks are damaged by the drilling and blasting excavation (D&B) or mechanical excavation (TBM) methods, and the physical and mechanical properties of surrounding rocks are changed. Thus, the excavation damaged zone (EDZ) is formed in surrounding rocks. After tunnel excavation, the stress in surrounding rocks is redistributed. The tangential stress continuously increases and leads to the development of EDZ from free surface to the deep. It often causes the spalling failure, large volume collapse, or even the rockburst, which seriously threatens the safety of life and property. Therefore, a thorough understanding of EDZ and its damage degree to surrounding rocks are an important guarantee to maintain the stability of tunnel.

In the following analysis, a tunnel with radius of $a$ was taken as an example to study the progressive failure process of surrounding rocks. Before analyzing the progressive failure process of surrounding rocks, since the sandstone specimen is firstly destroyed under the stress condition of $\sigma_{xi} = 0$ MPa and $\sigma_{xj} = 0$ MPa, the strength under this stress condition is taken as a reference in the following progressive

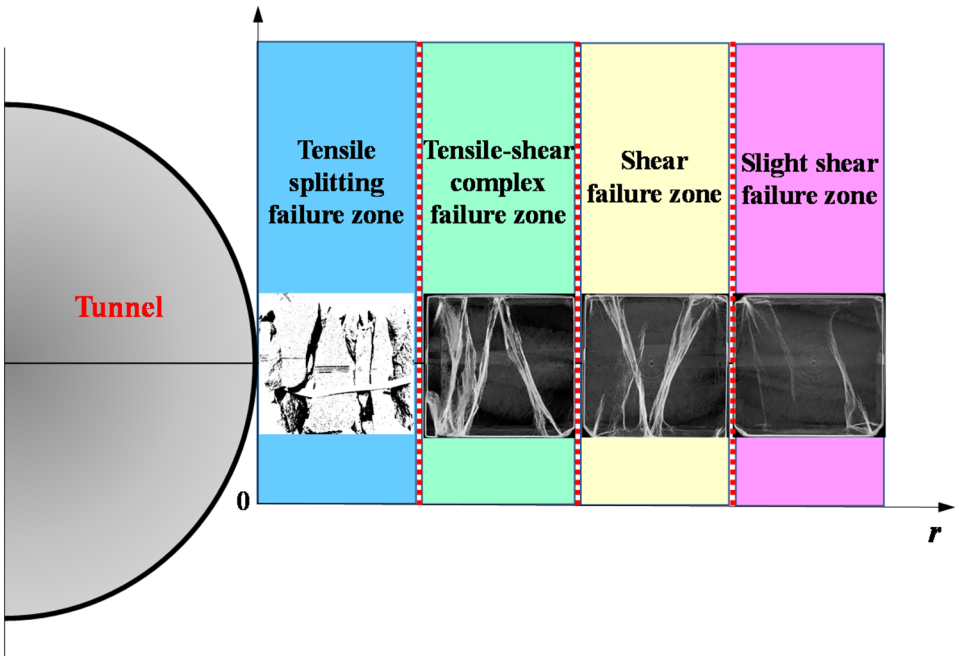


**Fig. 16** Schematic diagram of failure zone of surrounding rock in the radial direction

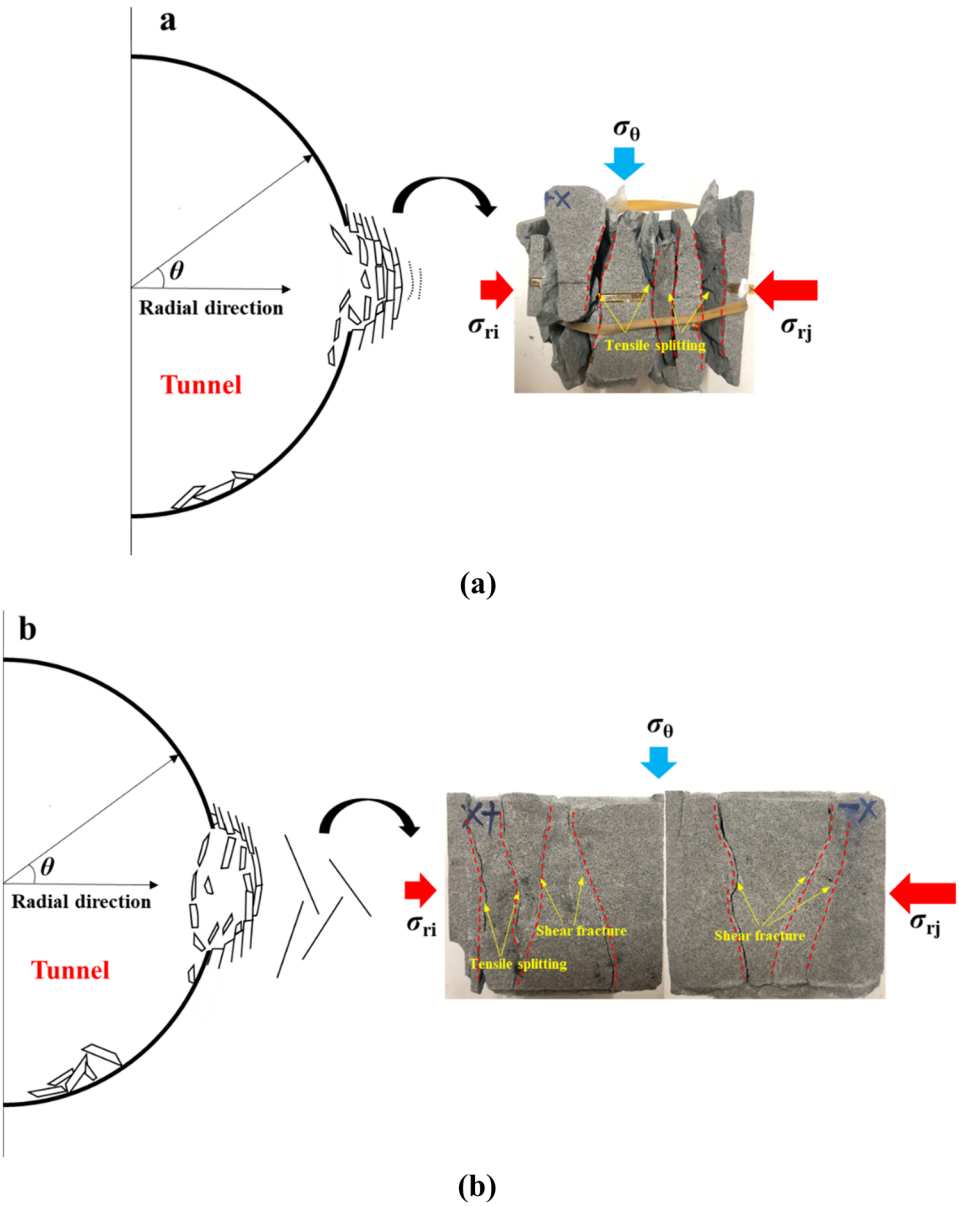


**Fig. 17** Schematic diagram of fracture mode of surrounding rock with different depths in the radial direction: **a** tensile splitting failure near the free surface; **b** shear fracture in deep surrounding rock

damage analysis. In addition, for convenience, the surrounding rock located at the surface of tunnel is referred to as No. 1 surrounding rock, and the surrounding rock within the range of $\sigma_{xi}=0$ MPa and $\sigma_{xj}=5$ MPa is referred to as No. 2 surrounding rock, and so on, as shown in Fig. 18.

In this study, the stress of crack initiation and propagation is taken as the starting point to calculate the EDZ of surrounding rock. When the tangential stress increases to 96.75 MPa, the surrounding rock at the free surface of tunnel are firstly destroyed by tensile splitting, and the damage has already been produced in No. 2 surrounding rock. According to the gradient distribution of radial stress, it can be inferred that the damage is mainly concentrated in the surrounding rock which is near the free surface. The radial stress in this part of the surrounding rock is small, and the rock is almost subjected to biaxial compression state. Thus, it is reasonable to infer that the failure mode of this part of the surrounding rock is tensile splitting failure. However, the tangential stress does not reach the bearing capacity of the surrounding rock which is far away from the free surface, and the overall failure of No. 2 surrounding rock does not occur, but the cracks in the rock are expanding unsteadily. At this moment, the depth of EDZ is 0.0383$a$. When the tangential stress increases to 108.45 MPa, No. 2 surrounding rock becomes unstable as a whole, and the failure mode is tensile-shear complex failure, while No. 3 surrounding rock and deeper surrounding rock are still in the elastic stage, and almost no damage is produced. The depth of EDZ is 0.115$a$. As the tangential stress continues to increase to 115.51 MPa, No. 3 surrounding rock enters the stage of unstable crack propagation, and

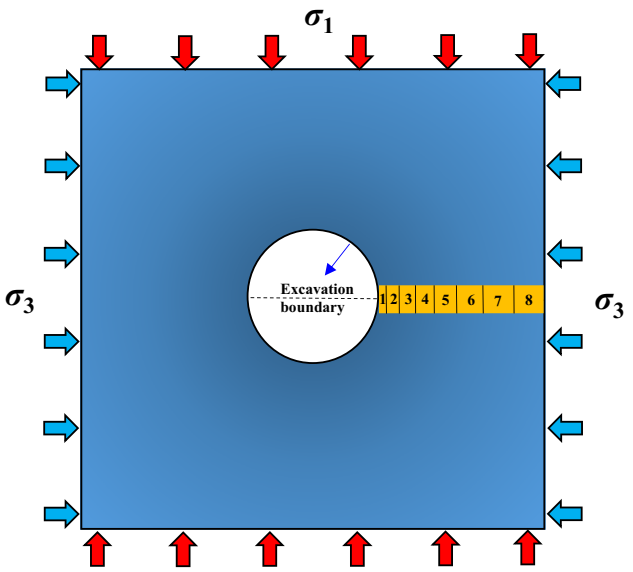


**Fig. 18** Marks of surrounding rock at different distances from free surface

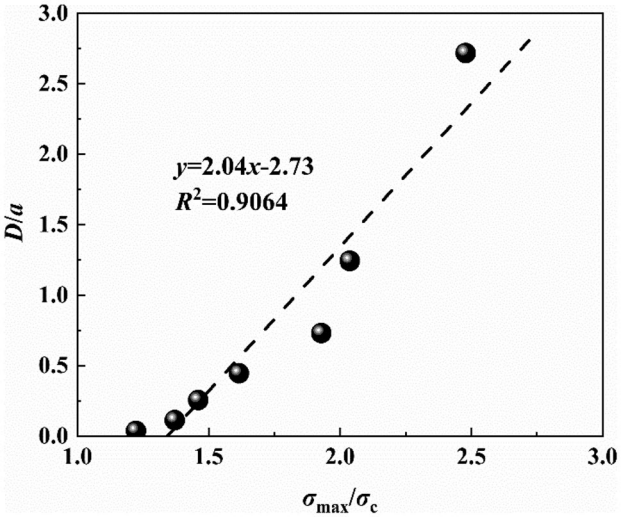


**Fig. 19** Relationship between tangential stress and depth of EDZ

the damage rapidly accumulates until shear failure occurs, and the depth of EDZ is 0.257$a$. With the increase of tangential stress to 127.74 MPa, No. 4 surrounding rock begins to fail at an accelerating rate, and No. 5 surrounding rock is still in the elastic stage. The depth of EDZ is 0.447$a$. Finally, when the tangential stress increases to 196.03 MPa, No. 1 ~ 6 surrounding rocks have failed. No. 7 surrounding rock is in the stage of crack stable expansion. The EDZ is close to the original rock stress area and equals to 2.717$a$. Since No. 8 surrounding rock is located in the original rock stress area, the range of this stress state is large. Thus, the damage range in this position is not considered in our study.

Through the above analysis, the damage of surrounding rocks in the radial direction is a progressive process in time and space. With the increase of the depth from free surface, the time needed for the damage of surrounding rocks gradually increases. The progressive process in space shows that the damage of surrounding rocks gradually develops from the free surface to the deep. The ratio of maximum stress $\sigma_{max}$ acting on the rock to the uniaxial compressive strength $\sigma_c$ can be used to characterize the difficulty of rock failure. According to the experimental results, we can get the relationship between the EDZ of surrounding rocks and the tangential stress acting on sandstone specimens, as shown in Fig. 19 and Eq. (6). Equation (6) is similar to the empirical formula proposed by Kaiser and Martin based on field tests. It can be seen that the area of EDZ of surrounding rocks is closely related to the mechanical properties of rock mass, tunnel size, and original rock stress. However, there are some gaps in the correlation coefficient, which may be caused by the homogeneity of the rock mass tested in the laboratory and the existence of end effect, resulting in the difference in the characteristic stresses between them and the in situ heterogeneous rock mass.

$$\frac{D}{a} = 2.04\frac{\sigma_{max}}{\sigma_c} - 2.73 \tag{6}$$

$$\frac{D}{a} = 1.34\frac{\sigma_{max}}{\sigma_c} - 0.57(\pm 0.05) \tag{7}$$

$$\frac{D}{a} = 1.25\frac{\sigma_{max}}{\sigma_c} - 0.51(\pm 0.1) \tag{8}$$

where $D$ is the depth of EDZ, $a$ is the equivalent radius of tunnel, $\sigma_{max}$ is the maximum tangential stress at the boundary of tunnel, and $\sigma_c$ is the uniaxial compressive strength of rock. Equations (7) and (8) are the empirical formula proposed by Kaiser and Martin, respectively.

## Time prediction of surrounding rock fracture under asymmetric radial stress conditions

In the aspect of preventing the rockburst and failure of tunnel surrounding rocks, it does not only need to monitor the stress distribution and deformation of surrounding rocks, but also need to predict the failure time according to the stress and the change law of deformation, so as to strengthen the support timely and effectively before the failure of surrounding rocks occurs. Due to the fact that the failure of surrounding rocks induced by the increase of tangential stress after tunnel excavation was simulated in this study. The rock

failure is essentially caused by the accumulation of damage under the effect of deviator stress. Thus, the time-failure model proposed by Voight can be used to predict rock failure (Voight 1988; Ying et al. 2009):

$$\frac{d^2\Omega}{dt^2} = A\left(\frac{d\Omega}{dt}\right)^{\alpha} \tag{9}$$

where $t$ is the real-time moment of the experiment recorded by the experimental apparatus in $s$, $A$ is the constant, $\alpha$ is an index to measure the degree of nonlinear, usually 1 ~ 2, and $\Omega$ is related to precursory strain. Based on the previous study, the minimum principal strain $\varepsilon_x$ is relatively sensitive to crack propagation (Kong et al. 2018) and is closely related to the failure of surrounding rock. Thus, $\varepsilon_x$ was used to reply $\Omega$ in our study, and Eq. (9) can be written as follows:

$$\frac{d^2\varepsilon_x}{dt^2} = A\left(\frac{d\varepsilon_x}{dt}\right)^{\alpha} \tag{10}$$

When the internal damage of rock accumulates to a certain extent, the cracks begin to rapidly expand out of control, and the rock begins to enter the stage of nonlinear expansion until rock failure, which exhibits a rapid increase of $\varepsilon_x$. At this moment, the value of $\alpha$ is equal to 2. Substitute it into Eq. (10):

**Table 5** Actual and prediction fracture times of sandstone specimen under different asymmetric radial stress conditions

| Number | $\sigma_{xi}$/MPa | $\sigma_{xj}$/MPa | Actual fracture time $t_{act}$/s | Prediction fracture time $t_{pre}$/s |
|---|---|---|---|---|
| S3 | 5 | 10 | 535.4 | 556.4 |
| S4 | 10 | 15 | 566.2 | 583.5 |
| S5 | 15 | 20 | 719.2 | 740.8 |
| S6 | 20 | 25 | 769.4 | 804.8 |
| S7 | 25 | 30 | 976.1 | 996.3 |
| S8 | 30 | 30 | 991.9 | 1044.5 |

$$\left(\frac{d\varepsilon_x}{dt}\right)^{-1} = \left(\frac{d\varepsilon_x}{dt}\right)_0^{-1} - A\left(t - t_0\right) \tag{11}$$

When the left side of Eq. (11) is equal to zero ($(d\varepsilon_x/dt)^{-1} = 0$), the line represented by Eq. (11) intersects with the abscissa, as shown in Fig. 20. It indicates that the cracks in the rock rapidly expand, coalesce with each other, and tend to failure. Take the test data into Eq. (11), and the predicted time of failure can be obtained. Table 5 lists the actual time of failure $t_{act}$ and predicted time of failure $t_{pre}$ under different asymmetric radial stress conditions. Note that $\varepsilon_x$ in the $\sigma_x$ cannot be measured under the stress condition of $\sigma_{xi} = \sigma_{xj} = 0$ MPa and $\sigma_{xi} = 0$ MPa, $\sigma_{xj} = 5$ MPa; thus,

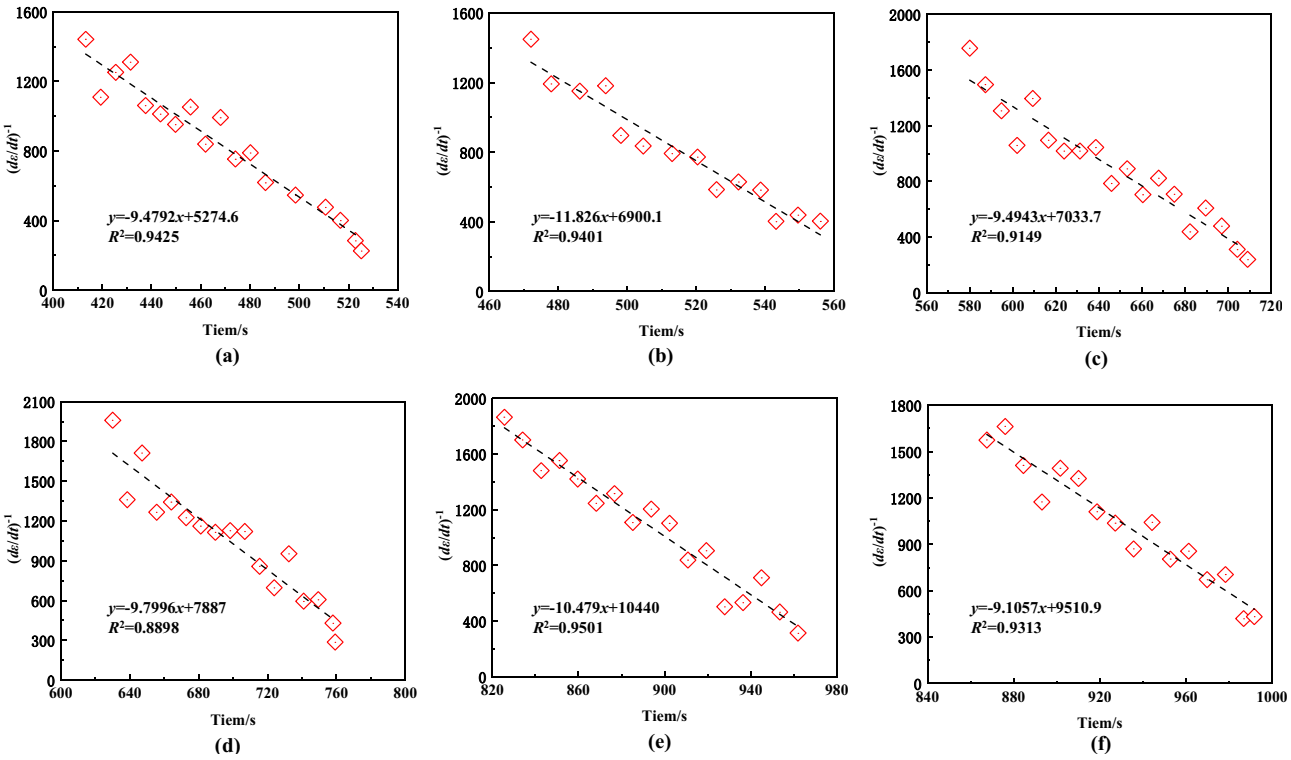


**Fig. 20** Prediction fracture time curves of sandstone specimen under different asymmetric radial stress conditions: **a** $\sigma_{xi} = 5$ MPa, $\sigma_{xj} = 10$ MPa; **b** $\sigma_{xi} = 10$ MPa, $\sigma_{xj} = 15$ MPa; **c** $\sigma_{xi} = 15$ MPa, $\sigma_{xj} = 20$ MPa; **d** $\sigma_{xi} = 20$ MPa, $\sigma_{xj} = 25$ MPa; **e** $\sigma_{xi} = 25$ MPa, $\sigma_{xj} = 30$ MPa; **f** $\sigma_{xi} = 30$ MPa, $\sigma_{xj} = 30$Mpa

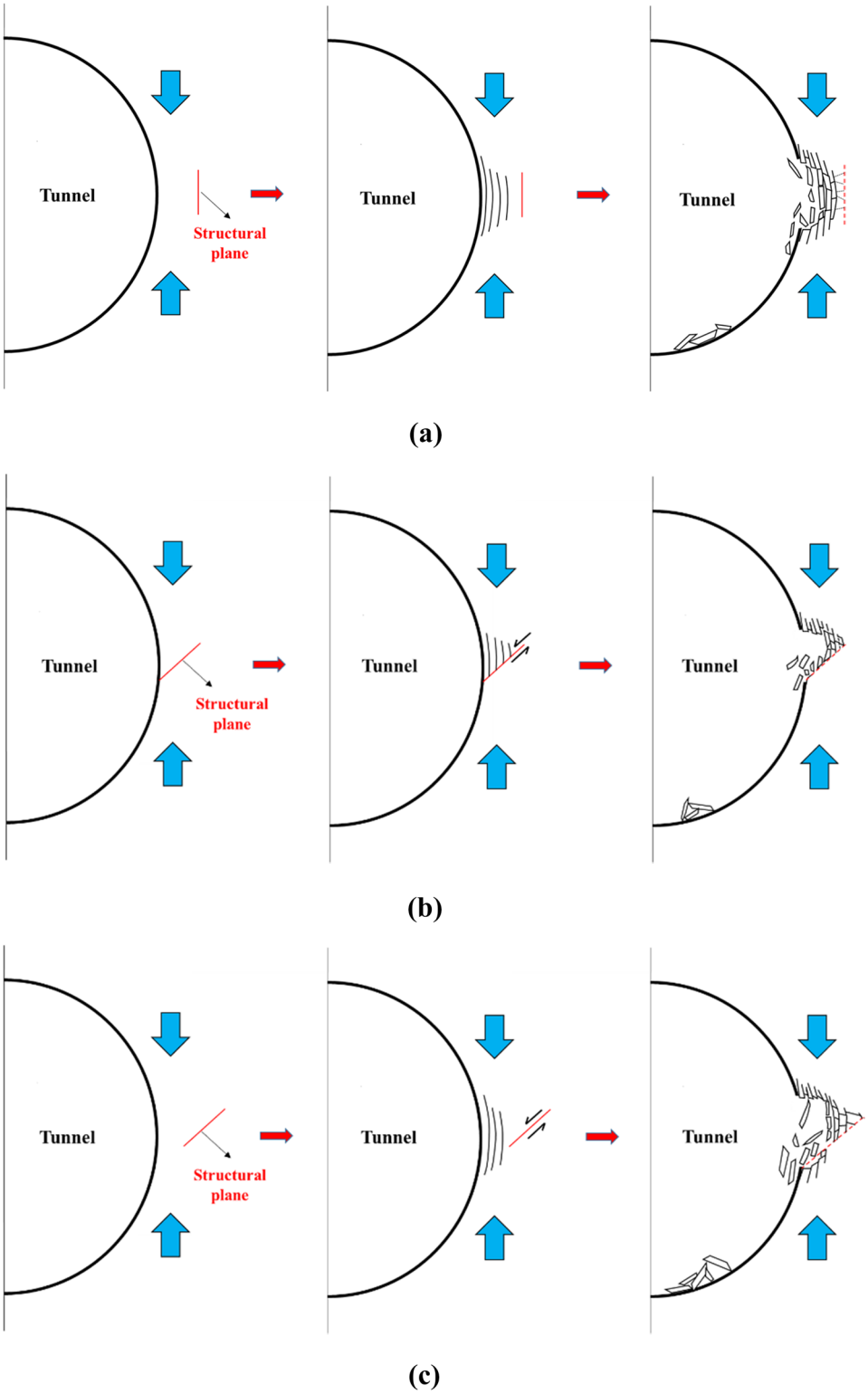


**Fig. 21** Sketch of mechanisms of structural plane in the formation of failure

the predicted time of failure is not shown in Table 5. It can be seen from the data in Table 5 that the predicted time $t_{pre}$ of failure is close to the actual time $t_{act}$ of failure, which implies that the time-failure model can be used to effectively predict the failure time of surrounding rocks. In practical engineering, the deformation and stress in the radial direction can be obtained by technical means. For example, by embedding optical fiber in surrounding rocks of tunnel, the distributed optical fiber monitoring technology is used to measure the stress and deformation (Chai et al. 2016; Yuan

et al. 2014), so as to predict the failure time of surrounding rocks and achieve the purpose of stress release or surrounding rock support in advance.

## Preliminary study on the influence of discontinuities on failure characteristics of surrounding rocks

Through the above test results and analyses, the tension cracks approximately parallel to the excavation surface are formed in the surrounding rock near the tunnel boundary. These tension cracks further expand, penetrate, and have tension displacement, cutting the surrounding rock into plate-shaped rock slab. After the tangential concentrated stress further acts on the rock plate and exceeds its ultimate strength, the rock plate will be unstable and damaged, forming rock mass ejection, while the failure of the surrounding rock far from the tunnel boundary are dominated by fracture. It should be noted that the test results in this paper are based on the intact rocks. Figures 16 and 17 show the failure mode of homogeneous and intact surrounding rock under the action of tangential concentrated stress. However, in the actual stratum, the rock mass often contains structural planes with different occurrences, location, and scale, showing significant deformation anisotropy. During the development of the failure from the rock mass near the tunnel boundary to the deep surrounding rock, the normal force of the structural plane gradually decreases, making the closed state of the structural plane change to active, and the structural plane begins to expand under the action of tangential concentrated stress. The failure of surrounding rocks is significantly influenced by the structural plane in this case. The influence of structural plane is illustrated below.

Case 1: When the structural plane is approximately parallel to the tunnel axis or distributed at a small included angle, as shown in Fig. 21a, the expansion of the fracture to the deep part of surrounding rocks is blocked and restricted by the structural plane, and the expansion of the structural plane further reduces the stability of the structure of surrounding rocks. In this case, the failure of surrounding rocks is mainly caused by the energy accumulation in the rock plate or external disturbance, and the structural plane controls the depth and shape of the failure of surrounding rocks.

Case 2: When the included angle between the structural plane and the tunnel axis is relatively large, as shown in Fig. 21b, the concentrated shear stress in the vertical direction can be decomposed into shear stress along the structural plane and normal stress perpendicular to the structural plane. When the shear stress applied to the structural plane is greater than its shear strength, the shear dislocation of the structural plane occurs, and the violent energy is released (Zhou et al. 2015a), which induces the overall instability and failure of surrounding rocks. Thus, the shear dislocation of structural plane becomes the inducing factor of the failure.

Case 3: For the unexposed structural plane, as shown in Fig. 21c, the rock mass between the structural plane and the tunnel boundary is still intact. After the excavation, the high shear stress is induced by the stress redistribution, resulting in shear dislocation along the structural plane. The intact rock mass between the structural plane and the tunnel boundary is subjected to shear failure, and the structural plane is connected with the tunnel boundary. During this failure process, the rigid filler or convex plate between the contact surfaces is sheared off. According to the research of (Ryder 1988; Zhou et al. 2015b), the stress decline caused by shear failure in weak planes such as structural plane is about 5 ~ 10 MPa, while the shear failure in intact rock mass is about 20 MPa, Therefore, it is reasonable to infer that the energy released in this failure process is greater than that in case 2 and less than the energy released by the failure of intact rock.

The above analyses are a preliminary understanding of the effect of structural plane on the failure of surrounding rocks based on the orientation and location of structural plane. However, in the actual stratum, the distribution of structural plane is random, and it has more complex morphology and different mechanical properties. Thus, it needs to be deeply analyzed and verified through laboratory tests, numerical simulation, and physical model tests.

## Conclusions

After tunnel excavation, the free surface was formed, and the radial stress in the surrounding rocks increased gradiently. In the non-principal stress space, the gradient characteristics of radial stress are simulated by applying different stresses on the front and back faces of cubic sandstone. The strength response and mechanism of fracture mode transformation were investigated. The main results can be concluded as follows:

1. Under different asymmetric radial stress conditions, with the increase in $\sigma_{xi}$ and $\sigma_{xj}$, the ductility of sandstone specimens performed more obviously, and the peak strengths of sandstone specimens gradually increased. That is to say, the properties of surrounding rocks show characteristics of transformation from brittleness to ductility with the increase of depth from the free surface. The relationship between the strength and the depth of surrounding rocks can be well described by a power function.
2. The fracture modes of sandstone specimens were significantly influenced by the asymmetric radial stress conditions, showing a transformation from tensile splitting fracture to tensile-shear complex fracture and finally to shear fracture with the increase of $\sigma_{xi}$ and $\sigma_{xj}$. Thus, four types

of failure zones in the radial direction can be divided, i.e., tensile splitting failure zone, tensile-shear complex failure zone, shear failure zone, and slight shear failure zone.

3. With the progressive failure of surrounding rocks, the excavation damage zone was gradually deepened and had a linear increasing relationship with the tangential stress. In addition, the time required for failure of sandstone specimens can be predicted by a time-failure model.

It should be pointed out that although the test results based on the intact rocks are different from the failure of surrounding rocks containing structural planes in the actual stratum, the failure modes in the tests are basically consistent with the existing research results. In addition, structural planes do not exist everywhere in surrounding rocks of the whole tunnel. Therefore, the research results of this paper are still helpful to understand the evolution process of the progressive damage failure and the mechanism of fracture mode transformation of surrounding rocks along the radial direction and can provide guidances for the stability control of surrounding rocks.

**Funding** This study was financially supported by the National Natural Science Foundation of China (51674049, 51674048).

## Declarations

**Ethics statement** It is not relevant to my work.

**Conflict of interest** The authors declare no competing interests.

## References

Alejano LR, Alonso E (2005) Considerations of the dilatancy angle in rocks and rock masses. Int J Rock Mech Min Sci 42:481–507. https://doi.org/10.1016/j.ijrmms.2005.01.003

Bishop A (1967) Progressive failure with special reference to the mechanism causing it. Paper presented at the Oslo: Proceedings of the Geotechnical Conference

Cai M (2008) Influence of intermediate principal stress on rock fracturing and strength near excavation boundaries—insight from numerical modeling. Int J Rock Mech Min Sci 45:763–772

Cai M, Kaiser PK, Tasaka Y, Maejima T, Morioka H, Minami M (2004) Generalized crack initiation and crack damage stress thresholds of brittle rock masses near underground excavations. Int J Rock Mech Min Sci 41:833–847

Chai J, Yuan Q, Li Y, Zhang D, Liu Q (2016) Experimental study on overlying strata deformation based on distributed optical fiber sensing. Chin J Rock Mech Eng 35:3589–3596

Chen W, Lu S, Guo X, Qiao C (2009) Research on unloading confining pressure tests and rockburst criterion based on energy theory. Chin J Rock Mech Eng 28:1530–1540

Diederichs M (2007) The 2003 Canadian Geotechnical Colloquium: mechanistic interpretation and practical application of damage and spalling prediction criteria for deep tunneling. Can Geotech J 44:1082–1116. https://doi.org/10.1139/T07-033

Feng XT, Gao Y, Zhang X, Wang Z, Zhang Y, Han Q (2020) Evolution of the mechanical and strength parameters of hard rocks in the true triaxial cyclic loading and unloading tests. Int J Rock Mech Min Sci 131:104349. https://doi.org/10.1016/j.ijrmms.2020.104349

Feng XT, Zhang X, Kong R, Wang G (2016) A novel Mogi type true triaxial testing apparatus and its use to obtain complete stress–strain curves of hard. Rock Mech Rock Eng 49:1649–1662. https://doi.org/10.1007/s00603-015-0875-y

Feng XT, Chen B, Zhang C, Li S, Wu S (2013) Mechanism, warning and dynamic control of rockburst development processes. Science Press, Beijing

Gong FQ, Luo Y, Li XB, Si XF (2017) Experimental modelling on rockburst in deep hard rock circular tunnels. Chin J Rock Mech Eng 36(7):1634–1648. https://doi.org/10.13722/j.cnki.jrme.2017.0160

Gong FQ, Luo Y, Li XB, Si XF, Tao M (2018) Experimental simulation investigation on rockburst induced by spalling failure in deep circular tunnels. Tunn Undergr Space Technol 81:413–427. https://doi.org/10.1016/j.tust.2018.07.035

Gong QM, Yin LJ, Wu SY, Zhao J, Ting Y (2012) Rock burst and slabbing failure and its influence on TBM excavation at headrace tunnels in Jinping II hydropower station. Eng Geol 124:98–108. https://doi.org/10.1016/j.enggeo.2011.10.007

Haimson B (2007) Micromechanisms of borehole instability leading to breakouts in rocks. Int J Rock Mech Min Sci 44:157–173. https://doi.org/10.1016/j.ijrmms.2006.06.002

Haimson B, Chang C (2000) A new true triaxial cell for testing mechanical properties of rock, and its use to determine rock strength and deformability of Westerly granite. Int J Rock Mech Min Sci 37:285–296. https://doi.org/10.1016/S1365-1609(99)00106-9

He M, Coli M, Livi E, Sousa L (2012a) Experimental study of rockbursts in underground quarrying of Carrara marble. Int J Rock Mech Min Sci 52:1–8. https://doi.org/10.1016/j.ijrmms.2012.02.006

He M, Miao J, Li D, Wang C (2007) Experimental study on rockburst processes of granite specimen at great depth. Chin J Rock Mech Eng 26(05):865–876

He M, Nie W, Zhao Z, Guo W (2012b) Experimental investigation of bedding plane orientation on the rockburst behavior of sandstone. Rock Mech Rock Eng 45:311–326. https://doi.org/10.1007/s00603-011-0213-y

He MC, Miao JL, Feng JL (2010) Rock burst process of limestone and its acoustic emission characteristics under true-triaxial unloading conditions. Int J Rock Mech Min Sci 47:286–298. https://doi.org/10.1016/j.ijrmms.2009.09.003

Hoek E, Martin CD (2014) Fracture initiation and propagation in intact rock – a review. J Rock Mech Geotech Eng 6:287–300

Horii H, Nemat-Nasser S (1985) Compression-induced microcrack growth in brittle solids: axial splitting and shear failure. Journal of Geophysical Research: Solid Earth 90:3105–3125

Hua AZ, You MQ (2001) Rock failure due to energy release during unloading and application to underground rock burst control. Tunn Undergr Space Technol 16:241–246. https://doi.org/10.1016/S0886-7798(01)00046-3

Huang D, Li Y (2014) Conversion of strain energy in triaxial unloading tests on marble. Int J Rock Mech Min Sci 66:160–168. https://doi.org/10.1016/j.ijrmms.2013.12.001

Jingtao C, Xiating F (2006) True triaxial experimental study on rock with high geostress. Chin J Rock Mech Eng 25(8):1537–1543. https://doi.org/10.1016/S1872-1508(06)60035-1

Jiang JQ (2017) Study on strainburst in tunnel using true-triaxial test and its kinetic energy prediction. Doctoral thesis Guangxi University (in Chinese)

Kong R, Feng XT, Zhang XW, Yang CX (2018) Study on crack initiation and damage stress in sandstone under true triaxial compression. Journal of Rock Mechanics and Mining Sciences 106:117–123

Li MH, Yin GZ, Xu J, Li WP, Song Z, Jiang C (2016) A novel true triaxial apparatus to study the geomechanical and fluid flow aspects of energy exploitations in geological formations. Rock Mech Rock Eng 49:4647–4659. https://doi.org/10.1007/s00603-016-1060-7

Luo Y, Gong F, Liu D, Wang SY, Si XF (2019) Experimental simulation analysis of the process and failure characteristics of spalling in D-shaped tunnels under true-triaxial loading conditions. Tunn Undergr Space Technol 90:42–61. https://doi.org/10.1016/j.tust.2019.04.020

Luo Y, Gong FQ, Li XB, Wang SY (2020) Experimental simulation investigation of influence of depth on spalling characteristics in circular hard rock tunnel. Journal of Central South University 27(3):891–910. https://doi.org/10.1007/s11771-020-4339-5

Li S, Feng XT, Li Z, Chen B, Zhang C, Zhou H (2012) In situ monitoring of rockburst nucleation and evolution in the deeply buried tunnels of Jinping II hydropower station. Eng Geol 137–138:85–96. https://doi.org/10.1016/j.enggeo.2012.03.010

Martin C (1997) Seventeenth Canadian geotechnical colloquium: the effect of cohesion loss and stress path on brittle rock strength. Can Geotech J 34:698–725. https://doi.org/10.1139/t97-030

Ortlepp WD (2001) The behaviour of tunnels at great depth under large static and dynamic pressures. Tunn Undergr Space Technol 16:41–48. https://doi.org/10.1016/S0886-7798(01)00029-3

Read R, Martin C (1996) Technical summary of AECL's Mine-by experiment, phase 1: excavation response. AECL

Ryder JA (1988) Excess shear stress in the assessment of geologically hazardous situations. J S Afr Inst Min Metall 88(1):27–39

Si X, Gong F (2020) Strength-weakening effect and shear-tension failure mode transformation mechanism of rockburst for fine-grained granite under triaxial unloading compression.Int J Rock Mech Mini Sci 131:104347. https://doi.org/10.1016/j.ijrmms.2020.104347

Stephansson O, Särkkä P, Myrvang A (1986) State of stress in Fennoscandia. In: Proceedings on Rock Stress and Rock Stress Measurement. Stockholm

Su G, Feng X, Wang J, Jiang J, Hu L (2017a) Experimental study of remotely triggered rockburst induced by a tunnel axial dynamic disturbance under true-triaxial conditions. Rock Mech Rock Eng 50:2207–2226. https://doi.org/10.1007/s00603-017-1218-y

Su G, Shi Y, Feng X-T, Jiang J, Zhang J, Jiang Q (2018) True-triaxial experimental study of the evolutionary features of the acoustic emissions and sounds of rockburst processes. Rock Mech Rock Eng 51:375–389. https://doi.org/10.1007/s00603-017-1344-6

Su G, Zhai S, Jiang J, Zhang G, Yan L (2017b) Influence of radial stress gradient on strainbursts: an experimental study. Rock Mech Rock Eng 50:2659–2676. https://doi.org/10.1007/s00603-017-1266-3

Voight B (1988) A method for prediction of volcanic eruptions. Nature 332:125–130

Wang B, Zhu J, Tan P, Huang S, Wu A (2012) Damage strength determination of marble and its parameters evaluation based on damage control tests. Chin J Rock Mech Eng 31:3967–3973

Xu H, Feng X-T, Yang C, Zhang X, Zhou Y, Wang Z (2019) Influence of initial stresses and unloading rates on the deformation and failure mechanism of Jinping marble under true triaxial compression. Int J Rock Mech Min Sci 117:90–104. https://doi.org/10.1016/j.ijrmms.2019.03.013

Ying WL, Benson PM, Young RP (2009) Laboratory simulation of fluid-driven seismic sequences in shallow crustal conditions. Geophysic Res Lett 36

Yuan Q, Chai J, Li Y, Zhang GH (2014) Experimental study on different forms of fiber Bragg grating sensors detecting for rock model test. In: Isrm Young Scholars Sympos Rock Mech 9–14

Yun X, Mitri H, Yang X, Wang Y (2010a) Experimental investigation into biaxial compressive strength of granite. Int J Rock Mech Min Sci 47:334–341. https://doi.org/10.1016/j.ijrmms.2009.11.004

Yun X, Mitri HS, Yang X, Wang Y (2010b) Experimental investigation into biaxial compressive strength of granite International. Journal of Rock Mechanics and Mining Sciences 47:334–341. https://doi.org/10.1016/j.ijrmms.2009.11.004

Zhao H, Liu C, Huang G, Yu B, Liu Y, Song Z (2020) Experimental investigation on rockburst process and failure characteristics in trapezoidal tunnel under different lateral stresses. Constr Build Mater 259:119530. https://doi.org/10.1016/j.conbuildmat.2020.119530

Zhao XG, Cai M (2010a) Influence of plastic shear strain and confinement-dependent rock dilation on rock failure and displacement near an excavation boundary. Int J Rock Mech Min Sci 47:723–738. https://doi.org/10.1016/j.ijrmms.2010.04.003

Zhao XG, Cai M (2010b) A mobilized dilation angle model for rocks. Int J Rock Mech Min Sci 47:368–384. https://doi.org/10.1016/j.ijrmms.2009.12.007

Zhao XG, Cai M (2014) Influence of specimen height-to-width ratio on the strainburst characteristics of Tianhu granite under true-triaxial unloading conditions. Can Geotech J 52(7):890–902. https://doi.org/10.1139/cgj-2014-0355

Zhou H, Xu RC, Lu JJ, Zhang CQ, Meng FZ, Shen Z (2015a) Study on mechanisms and physical simulation experiment of slab buckling rockburst in deep tunnel. Chin J Rock Mech Eng 34(S2):3658–3666

Zhou H, Meng FZ, Zhang CQ, Lu JJ, Xu RC (2015b) Effect of structural plane on rockburst in deep hard rock tunnels. Chin J Rock Mech Eng 34(4):720–727